In situ fractional crystallization of a mafic pluton: Microanalytical study of a Palaeogene gabbronorite plug in East Greenland

Stefan Bernstein *

Geological Survey of Denmark and Greenland, Øster Voldgade 10, 1350 Copenhagen K, Denmark

Abstract

Spot analysis techniques have been used to unravel crystallization processes in a Palaeogene coarse-grained, olivine-bearing, gabbronoritic plug from East Greenland. Whole-rock analyses of the gabbronorite and its chilled margin are identical to within analytical error, yet the gabbronorite is coarse-grained and has large, strongly zoned pyroxene, olivine and plagioclase crystals. The textures of both the gabbronorite and its chilled margin suggest high crystal growth rates. Electron- and ion-microprobe and LA–ICP–MS analyses of clinopyroxene crystals reveal a complex zonation pattern, with a large core segment dominated by oscillatory zoning, and strong normal zoning towards the rim. The general zoning pattern of Fe–Mg and Sr, Ti, Cr, Ce, Y, and Zr in clinopyroxene and orthopyroxene can be explained in terms of fractional crystallization of the four-phase assemblage plagioclase–clinopyroxene–orthopyroxene–olivine, with phase proportions similar to the mode of the gabbronorite. The oscillatory zoning of clinopyroxene is most likely a result of the development of transient chemical boundary layers between the fast-growing clinopyroxene crystal and the bulk melt reservoir. Calculated melt compositions in equilibrium with clinopyroxene cores from the gabbronorite are close to the composition of the chilled margin for most elements, thus lending support to this approach for estimating the composition of melts parental to plutonic rocks, in which post-cumulus equilibration with migrating interstitial melts is limited.
© 2006 Elsevier B.V. All rights reserved.

1. Introduction

Studies of mafic and ultramafic cumulate rocks are traditionally based on two different viewpoints. One is the wish to understand the nature and origin of textural and structural features, most prominently the conspicuous layering in many mafic and ultramafic plutons (e.g. Wager and Brown, 1968; Parsons, 1987; Cawthorn, 1996a) and how these are related to the crystallization processes during cooling of the pluton (Wager and Deer, 1939; McBirney, 1998). The other is the wish to obtain information on the composition and evolution of the melt(s) from which the cumulate rocks crystallized. The melt composition can be used to evaluate the origin of the mafic–ultramafic complexes, and as a tool to understand regional petrogenetic processes (e.g. Barnes, 1989; Kelemen et al., 1997). If contamination with foreign material during crystallization can be excluded, then age-corrected radiogenic isotope ratios (typically Pb, Sr, and Nd) will be representative of the melt at the time when the pluton was emplaced. In addition to the

---

* Tel.: +45 38142271; fax: +45 142050.
  E-mail address: sb@geus.dk.

isotope systems, information of the trace element composition of the parent melt is of particular interest to petrogenetic characterization and modelling. The term 'parent melt' is here defined as the composition of the melt at the time of emplacement, but before fractionation and/or contamination processes took place within the magma chamber.

In the search for a parent melt composition, a series of different methods have been employed, such as using chilled margins (Wager, 1960; Hoover, 1978), intraplutonic quench zones (Tegner et al., 1993) and contemporaneous dykes associated with the intrusion (Brooks and Nielsen, 1978). Although successful in many instances, these approaches suffer from a common drawback, namely the assumption that the selected rock samples are truly representative of the melt from which the cumulates of interest crystallized. To supplement the above methods it is often advantageous to focus on the chemistry and petrology of the cumulate rocks themselves. As described and discussed by Bédard (1994) there are three commonly used methods for obtaining information on the trace element composition of the parent melt based on cumulate samples:

(a) Analysis of bulk-rock chemistry in combination with mineral modes and distribution coefficients to calculate composition of the melts in equilibrium with the observed minerals. This requires that accessory phases can be correctly accounted for, and the mode accurately determined, which is not trivial in coarse-grained rocks, and that the effects of trapped melt are considered (Barnes, 1986; Harnois et al., 1990; Bédard, 1994; Benoit et al., 1996).

(b) Analysis of mineral separates together with distribution coefficients can be used to calculate the equilibrium melt composition. This approach is severely hampered by the difficulty in obtaining clean mineral separates free of accessory phases, in particular those with distinct trace element profiles such as apatite and titanite. Another potential complication is crystallization of trapped melt at grain edges, which will affect the calculated equilibrium melt composition considerably (Benoit et al., 1996).

(c) In situ analysis of major and trace elements in minerals together with distribution coefficients can be used to calculate the equilibrium melt composition. The advantage of this method over the first two mentioned is that the risk of including 'impurities' in the mineral analysis is much reduced, and that it also provides valuable information on the crystallization of the rock. The requirement for correctly estimating the parent melt composition is that the crystal cores of phases that crystallize early are analysed in order to minimize the effects of any in situ fractionation processes.

This paper addresses the 'in situ analysis' approach, since this method is widely used (and increasingly so with the current advances in spot analysis techniques), combining major element data on solid phases from the electron-microprobe with either ion-microprobe or laser ablation ICP–MS analyses (e.g. Vannucci et al., 1993; Kelemen et al., 1997; Bernstein et al., 1998, Eggins et al., 1998; Normann, 1998). Based on major and trace element data on cumulus clinopyroxene cores in a coarse grained gabbronorite from Courtauld Fjord, East Greenland, calculated parent melt composition is compared with the composition of the chilled margin of the intrusion. The small size of the Courtauld Fjord plug and the homogenous nature of the gabbronorite, which suggests that it crystallized from a single pulse of magma, makes this igneous body ideal for the study of parent melt composition, since complicating factors such as magma-mixing and post-emplacement contamination can be ruled out. The gabbronorite has a bulk-rock composition that, within analytical error, is identical to its chilled margin, both in terms of element concentrations and Sr and Nd isotope ratios. All processes recorded in the minerals must therefore reflect closed-system conditions at the scale of the whole rock sample (10 cm), which in turn places important constraints on the origin of zoned crystals in the gabbronorite.

2. Geology

The Courtauld Fjord intrusion (68°25.70′N; 32°14.00′W) is an undeformed mafic plug of Palaeogene age intruded into ca. 3.0 Gy Precambrian gneisses (Kays et al., 1988). It is ca. 200 m across at sea level, with a vertical exposed extent of nearly 400 m (Fig. 1). It consists mainly of coarse-grained, olivine-bearing, gabbronorite, which towards the north is intruded by fine-grained olivine gabbro. Both units are unlayered and homogeneous. The contact between the olivine gabbro and the gabbronorite is locally sharp and clearly intrusive, whereas elsewhere it appears more gradational. While the northern contact of the plug is obscured by moraine, there is good exposure of the southern contact between the gabbronorite and the gneissic basement. The contact rock is a 1.0- to 1.5-m-thick chilled zone consisting of diabase. Dendritic clinopyroxene and
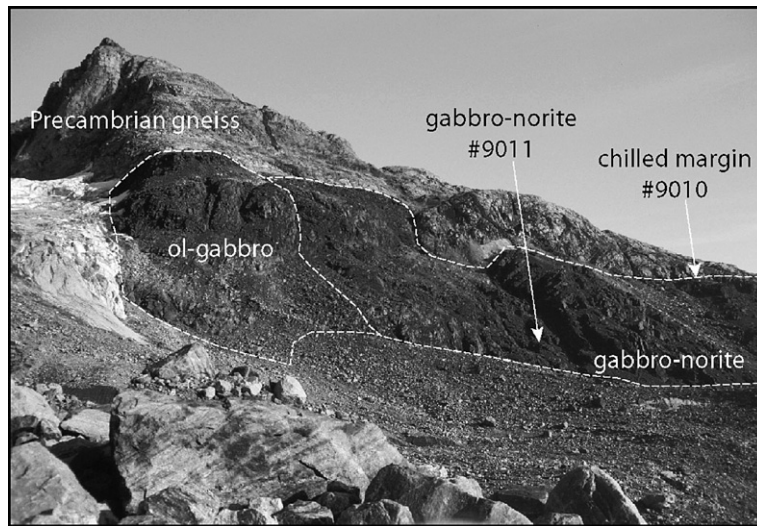
Fig. 1. Photograph of Courtauld Fjord plug, taken from the coastline looking east. The Courtauld Fjord plug is located in southeast Greenland at 68°25.70′N, 32°14.00′W. The two samples were taken from the gabbronorite body, which occupies the southern part of the plug and terminates at about 400 m elevation against the hosting Precambrian gneisses. Sample #9010 is from a 1- to 1.5-m-wide chilled margin of the coarse-grained olivine gabbronorite (#9011).

olivine crystals oriented perpendicular to the contact occur locally in addition to small clusters of olivine crystals.

The exposed roof of the intrusion shows complex outcrops of gabbronorite intruded by basaltic dykes and cut by small-scale faults and carbonate-mineralized breccia zones. The plug was originally described by Wager (1947) as a volcanic neck, and the present field observations would seem to support this view of a shallow level intrusion which probably represents a magmatic conduit system.

3. Petrography

The olivine gabbronorite sample (#9011) is a coarse-grained rock, taken ca. 80 m from the southern contact (Fig. 1). It has an approximate modal composition of 50% plagioclase, 30% clinopyroxene, 10% orthopyroxene, 10% olivine and a few percent amphibole, biotite and opaque phases, determined by area measurements in two thin sections. The largest clinopyroxene and plagioclase crystals are about 7 mm across and euhedral, whereas the largest olivine and orthopyroxene crystals are about 6 mm across. Orthopyroxene is mostly euhedral, and olivine subhedral. The texture shows clusters (to 8 mm across) of individual blade-shaped clinopyroxene crystals radiating from the centre of the clusters (Fig. 2a and b). The centres of these clusters consist of fine-grained intergrowths of clinopyroxene,

olivine, orthopyroxene and sparse plagioclase (see insert in Fig. 2). Orthopyroxene occurs in the centre of some of the clinopyroxene clusters, but it mainly forms distinct crystals between the clusters. No exsolution textures were visible optically in either of the pyroxenes. The sample appears isotropic in terms of texture, with no preferred orientation of crystal laths.

All crystals were found to be zoned. The clinopyroxene blades show optically concentric zoning from the centre of a cluster towards the edges (Fig. 2a). Orthopyroxene and the larger euhedral plagioclase crystals show optical zoning, whereas the larger olivine crystals show only weak optical zoning. For all crystals it was found that the zoning was most intense near the crystal margin.

Fine-grained biotite, amphibole, apatite and Fe–Ti oxide are found intergrown with clinopyroxene and plagioclase in irregular pockets 1–2 mm in diameter, scattered throughout the sample, often in interstices between larger crystals (Fig. 2b and d). In addition, fine-grained biotite and amphibole locally form rims on clinopyroxene crystals.

Sample #9010 of the chilled margin comes from a portion without obvious dendritic pyroxenes or olivines. The sample has sparse olivine and orthopyroxene microphenocrysts up to 1 mm long, set in a fine-grained groundmass of plagioclase, clinopyroxene, orthopyroxene and olivine (Fig. 2c). Larger anhedral plagioclase crystals up to 3 mm in length occur frequently,
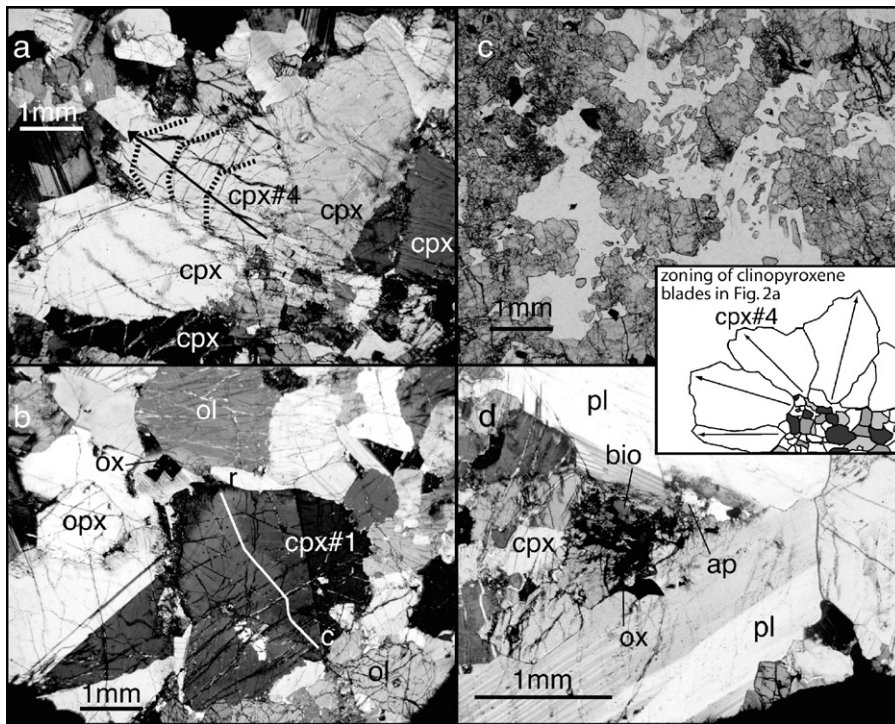
Fig. 2. (a and d) Photomicrograph of textures. (a) (XPL) gabbronorite #9011 showing group of zoned clinopyroxene crystals, radiating from a fine-grained cluster of clinopyroxene, olivine and plagioclase grains. Stippled lines show the typical zoning structure, and arrow gives direction of zoning from core (c) to rim (r) and represent also the location of the LA–ICP–MS line scan. Insert shows the arrangement of zoned clinopyroxene blades in panel (a). (b) (XPL) #9011 with analysed clinopyroxene crystal cpx#1 and showing euhedral orthopyroxene and subhedral olivine. Note also the euhedral spinel crystals (ox) in the intersticie between cpx#1, and the olivine and orthopyroxene crystals. Line c (core) to r (rim) shows the electron microprobe traverse reported in Fig. 3. (c) (PPL) chilled margin sample #9010. (d) (XPL) interstitial material between plagioclase laths in gabbronorite #9011, with fine-grained intergrowth of clinopyroxene, plagioclase, Fe–Ti oxide, biotite, and apatite.

poikilitically enclosing groundmass pyroxene and olivine grains.

4. Analytical technique

Samples of the chilled margin (#9010) and gabbronorite (#9011) had their altered surfaces removed prior to crushing in an agate mortar. Major element concentrations were determined by XRF on fused glass disks, FeO by titration, and Na₂O by AAS at The Geological Survey of Denmark and Greenland's (GEUS) Rock Geochemical Laboratory (Kystol and Larsen, 1999). Trace elements were determined by ICP–MS at Oregon State University and at GEUS using BIR-1, W-2, BHVO-1, BE-N and BR as calibration standards. The uncertainties are less than 1% (relative) for the major elements and around 5% (relative) or less for the reported trace elements.

Several thin sections were made of the coarse-grained gabbronorite #9011. Major elements of

minerals were analysed using the JEOL electron-microprobe at the Geological Institute, University of Copenhagen. All elements were measured by EDS (120 s count time), except Cr, Ni and Na, which were analysed by WDS (40 s peak count time for Cr and Ni, and 20 s peak count time for Na). The trace elements Ti, Cr, Sr, Y and Zr, together with eight rare earth elements (REE) were measured on one clinopyroxene crystal (cpx#1), and Ti, Cr, Y and Zr were measured in one orthopyroxene crystal (opx#2) using the Cameca 3f ion-microprobe at the Woods Hole Oceanographic Institution. The standard technique was followed as described by Shimizu and Hart (1982), using a beam diameter of 10–15 μm. The errors are better than 5% for the more abundant trace elements and around 10% for the REEs. Due to the low abundance, errors for determining Y and Zr in orthopyroxene are around 10%. The accuracy was monitored by repeated analyses of the clinopyroxene standard KH-1.

In addition, one clinopyroxene crystal (cpx#4) was analysed for trace elements and Si, Ca, Mg and Fe by laser ablation ICP–MS (LA–ICP–MS) using the Elan DRC 2000 Sciex Quadropole ICP–MS at GEUS, equipped with a Cetax LSX-200 frequency quadrupled (266 nm) Nd:YAG laser. The laser was operated in Q-switched mode with a pulse rate of 3 ns. Beam size was 100 μm and focussed at the sample plane. Laser energy level was set to maximum and pulse repetition was set to 20, resulting in yielded laser energy of 7.5 mJ. The clinopyroxene was analysed along a 3.8 mm long line along which the laser beam moved 3 μm/s. The data was corrected for blanks, as counted on the Ar carrier gas alone, and then normalized to Ca, as obtained by electron-microprobe. Calibration curves were constructed using BHVO2g, BCR2g and NIST610 glass standards and accuracy was monitored by analysis of our in-house clinopyroxene standard BB2. Standards and unknowns were measured with identical machine set-up: 100 replicates were chosen for glass standards, resulting in a line scan of about 1 mm length. 50 replicates were chosen for clinopyroxene standard BB2, equaling a 0.5 mm line scan. For the trace

elements with abundances >10 ppm the errors are about 5%, while for elements with abundances at the 1 ppm level, the typical error is about 10%.

The elements Fe, Mg, Cr and Ti were measured both by the ion- and electron-microprobes. For Mg# and for Cr and Ti less than about 3000 ppm, data obtained by the two methods agree within error. For Cr and Ti concentrations higher than about 3000 ppm, the electron- and ion-microprobe results diverge appreciably, with the apparent concentrations being consistently lower for the ion-microprobe measurements by some 15–30% (Table 2). This inconsistency could be explained by the fact that although great care was taken to analyse the same spot with the two techniques, a small offset in a zoned crystal could result in considerable compositional variations. This is illustrated in the concentration profile over the clinopyroxene crystals cpx#1 (Fig. 3e, f) and cpx#4 (Fig. 5a, c). On the other hand, the very good agreement for the low concentration crystal domains, as well as the consistently lower concentrations for the ion-probe data when analysing domains with higher concentrations, suggest an analytical bias for the ion-microprobe, when
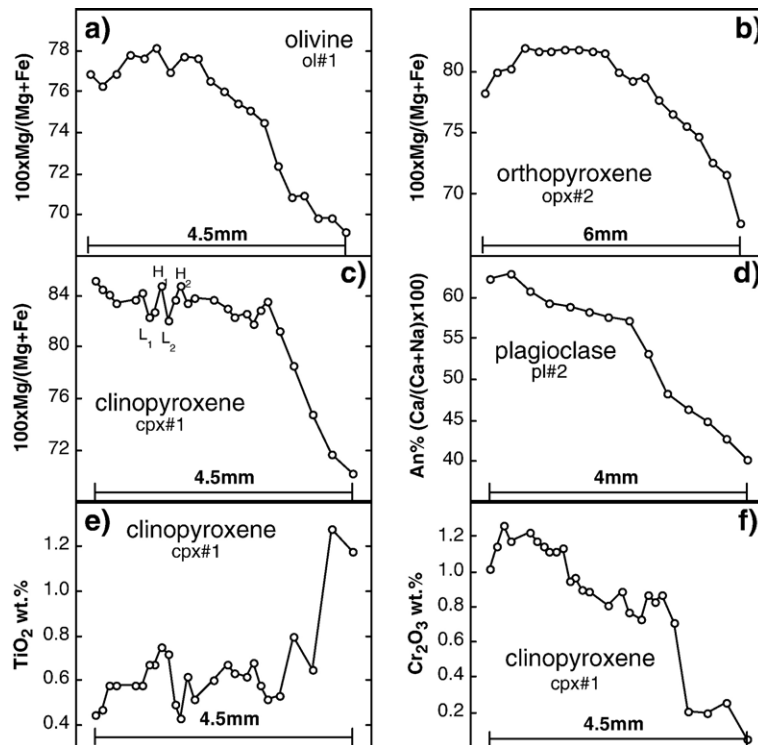

Fig. 3. (a)–(f) Zoning patterns of minerals in gabbronorite #9011 as analysed by the electron microprobe. Core to rim traverses from left to right, respectively: (a) Mg# in olivine. (b) Mg# in orthopyroxene. (c) Mg# in clinopyroxene. L_1, L_2, H_1 and H_2 correspond to similar low (L) and high (H) spikes in Fig. 5d. (d) An% in plagioclase. (e and f) show variation in TiO_2 and Cr_2O_3 for clinopyroxene#1 (cpx#1 in Fig. 2b).

analysing >3000 ppm Cr and Ti. This could arise from errors in the empirical calibration curves when calculating concentrations from counts per seconds. Secondary standards used during electron-microprobe analyses show errors of less than 5% relative for Cr and Ti in the range 1.0–0.1 wt.% (corresponding roughly to the range 6000–600 ppm). For the high Cr and Ti concentrations in cpx#1 and opx#2, electron-microprobe data have therefore been used in the discussion below, while for low concentrations, ion-microprobe data was used.

For the whole rock isotope analyses, ca. 50 mg of sample powder was digested in a mixture of 4 : 1 HF/HClO$_4$ at 100 °C, leaving no residue. Rb, Sr, Sm, and Nd were separated using ion exchange columns, following established methods at the Woods Hole Oceanographic Institution. The isotopic measurements were carried out using a VG 354 multi collector. NBS 987 and La Jolla standards yielded ^{87}Sr/^{86}Sr values of 0.710245–0.710278 and ^{143}Nd/^{144}Nd values of 0.511838–0.511859 during the time of measurements.

5. Analytical results

As is evident from Table 1, the whole rock compositions of the chilled margin #9010 and the gabbronorite #9011 are identical within the error of the analyses except for Cr and Ni, which in #9010 are 66% and 16% (respectively) of the contents in the gabbronorite. Similarly, age-corrected Sr- and Nd-isotopic ratios are very close to one another for the two samples, with relatively radiogenic Sr-isotopes (^{87}Sr/^{86}Sr>0.707) and unradiogenic Nd isotopes (ε_{Nd} of about −4.7).

Zonation patterns in Mg–Fe of olivine, ortho- and clinopyroxene and in Ca–Na of plagioclase are shown in Fig. 3. The clinopyroxene crystal shows strong zoning in the outer 1 mm, whereas the olivine and orthopyroxene crystals are strongly zoned in the outer 1 to 2 mm. However, these apparent thicknesses are dependent on the orientation of the crystal relative to the plane of the thin section. There is relatively good agreement between Fe/Mg K_D among the ferromagnesian phases. Using the maximum Mg# of the olivine (78.1), and the maximum Mg# in the orthopyroxene crystal core (81.5), the K_D for the exchange of Mg–Fe between orthopyroxene and olivine is 1.25. This is only slightly higher than the experimentally determined K_D of 1.03 to 1.18 at 1.0–2.5 GPa and 900–1100 °C (Brey and Köhler, 1990). For clinopyroxene, the maximum Mg# (assuming all iron as Fe^{2+}) is around 84, giving a clinopyroxene–olivine K_D of 1.47 for the olivine Mg#

of 78.1. This is within the range of values (1.04–1.91) reported by Brey and Köhler (1990). Large plagioclase crystals show normal zoning styles with large ranges in chemical composition (62.8% to 40.3% anorthite; Fig. 3d).

The clinopyroxene blades are also zoned with respect to minor and trace elements. For Cr$_2$O$_3$ and TiO$_2$, concentrations in the cpx#1 core are around 1.2 and 0.5 wt.%, respectively (corresponding to 8000 ppm Cr and 3000 ppm Ti, respectively; Fig. 3e and f, and Table 2), and correlate with Mg# in the way shown for cpx#1 and cpx#4 in Fig. 4. The rim of cpx#1 shows an extreme enrichment in titanium (to >1.2 wt.% TiO$_2$ or >7000 ppm Ti) and corresponding depletion in chromium (to <0.05 wt.% Cr$_2$O$_3$ or <400 ppm Cr). For the trace elements Zr, Y and the REEs, the variations between crystal core and crystal rim are similar (Table 2), with enrichment factors (rim/core) of 3.3 (Zr), 3.1 (Nd), 2.7 (Ti), 2.9 (Y), while for Sr the enrichment is modest (1.25).

For clinopyroxene crystal cpx#4, which was analysed by LA–ICP–MS with the laser in line-scan mode, the zoning pattern is similar to that of cpx#1 (Figs. 4 and 5a–h). Mg# variation in cpx#4 corresponds closely to that of cpx#1 (compare Fig. 3c with Fig. 5d), with a broad zone of variable and high Mg# (>85) followed by a drop at the outer 0.5 mm to very low Mg# of about 72. This general relationship is followed either directly or inversely by all trace elements except for Sr, which shows a less distinct zoning pattern with an increase at the rim, but has three equally high peak concentrations within the crystal (Fig. 5a). The core and rim analyses of cpx#1 show good agreement with the line scan of cpx#4 (Fig. 5a–h), particularly for the core analysis. The cpx#1 rim data are more extreme than those of cpx#4 for some elements. For example, the cpx#1 rim shows significantly lower Mg# values and Cr and Dy concentrations, whereas Ti, Ce and Zr are significantly higher than in the cpx#4 rim.

The data for orthopyroxene opx#2 show a similar variation between core and rim as for cpx#1, with enrichment factors of 3.7 (Zr), 3.1 (Ti) and 2.4 (Y). Distribution of trace elements between clinopyroxene and orthopyroxene cores (Table 2) shows that the clinopyroxene/orthopyroxene distribution coefficients calculated here are very close to recommended values from the literature (Table 3). With the value calculated from published K_D given in parentheses (references in Table 3), the values are: Ti: 2.1 (2.7); Y: 4.9 (4.7); Zr: 5.4 (6.2); and Cr: 2.2 (2.4). This implies that clinopyroxene and orthopyroxene cores crystallized in mutual equilibrium, in accordance with the distribution

Table 1
Major and trace element composition of gabbronorite chilled margin (#9010) and gabbronorite (#9011) together with melt calculated to be in equilibrium with clinopyroxene core cpx#1

Sample no. (wt.%)	9011wr	9010wr	9011cpx#1 core	9011 eq. liq.	Deviation in % calculated equilibrium melt − #9010 chilled margin
SiO_2	51.00	51.63	52.66		
TiO_2	1.14	1.14	0.45		
Al_2O_3	7.59	7.59	1.79		
Fe_2O_3	10.01	1.08			
FeO	8.19				
FeO(total)	9.01	9.16	5.72		
MnO	0.17	0.18	0.08		
MgO	14.68	14.38	18.78		
CaO	12.56	12.95	18.97		
Na_2O	1.50	1.45	0.27		
K_2O	0.44	0.37			
P_2O_5	0.11	0.09			
Cr_2O_3	1.18				
Volatility	0.11	1.00			
Sum	99.31	100.04	99.9		
Mg# (ppm)	74.4	75.7	85.2	59.9	
Ti	6810	6834	2698	7026	3
Rb	8.1	6.4			
Ba	153	144			
Sr	162	161	17.6	135	−16
Y	13.7	15	6.4	14	−9
Zr	81	73	9.2	75	2
Zn	85	83			
Cu	70	69			
Ni	370	318			
Sc	46	46			
V	300	318			
Cr	3330	2200	8074	2125	−3
Ga	13	15			
La	9.4	8	0.52	9.63	20
Ce	22.3	23	2.11	25.12	9
Nd	12.4	15.5	2.71	14.41	−7
Sm	3.0	2.9	1.07	3.68	27
Eu	0.9	0.9	0.28	0.97	7
Tb	0.5	0.5			
Dy	2.9	2.7	1.21	2.75	2
Er	1.4	1.5	0.62	1.60	7
Yb	1.1	1.2	0.51	1.19	−1
Lu	0.2	0.2			
Hf	1.8	1.7			
La(N)[a]	39.7	33.8		40.6	
Ce(N)	36.4	37.6		41.0	
Nd(N)	26.6	33.2		30.9	
Sm(N)	19.6	19.0		24.0	
Eu(N)	16.0	15.5		16.6	
Dy(N)	11.2	10.6		10.8	
Er(N)	8.5	9.1		9.7	
Yb(N)	6.6	7.1		7.0	
$^{87}Sr/^{86}Sr_m$	0.707501	0.707485			
$^{87}Sr/^{86}Sr_i$	0.707402	0.707406			
$^{143}Nd/^{144}Nd_m$	0.512381	0.512373			
$^{143}Nd/^{144}Nd_i$	0.512333	0.512336			
ε_{Nd} 50 Ma	−4.70	−4.65			

Uncertainty for $^{87}Sr/^{86}Sr$ is ±0.000008 and for $^{143}Nd/^{144}Nd$ ±0.000010 (2 s).

[a] REE chondrite-normalised (Sun and McDonough, 1989).

Table 2
Major and trace element composition of pyroxenes from olivine gabbronorite #9011

wt.%	Clinopyroxene cpx#1		Orthopyroxene opx#2			Observed K_D
	Core	Rim	Core	Middle	Rim	cpx/opx cores
Shot #	162	130	100	89	85	
Na$_2$O	0.28	0.32	0.02	0.05	0.05	
MgO	19.02	15.53	28.74	26.56	23.29	
Al$_2$O$_3$	2.08	2.31	1.49	0.83	0.66	
SiO$_2$	52.38	51.82	54.67	54.58	52.42	
CaO	18.43	17.59	2.34	2.17	2.01	
TiO$_2$	0.45	1.20	0.21	0.33	0.65	
Cr$_2$O$_3$	1.18	0.05	0.54	0.07	0.03	
MnO	0.26	0.01	0.28	0.30	0.37	
FeO	5.66	11.68	11.27	15.04	19.50	
NiO	0.01	0.05	0.01	0.07	0.04	
Sum	99.58	100.49	99.54	99.93	98.97	
Formula based on 4 cations						
Si	1.912	1.922	1.952	1.972	1.954	
Al(IV)	0.088	0.078	0.049	0.028	0.029	
Al(VI)	0.002	0.023	0.014	0.007	0.000	
Ti	0.012	0.033	0.005	0.009	0.018	
Cr	0.029	0.002	0.015	0.002	0.001	
Fe$_2$	0.121	0.351	0.326	0.450	0.579	
Fe$_3$	0.052	0.012	0.010	0.005	0.029	
Mn	0.008	0.000	0.009	0.009	0.012	
Mg	1.035	.859	1.530	1.431	1.295	
Ca	0.721	0.699	0.090	0.084	0.080	
Na	0.020	0.023	0.001	0.004	0.004	
Mg# (Fe$_{tot}$)	85.70	70.33	81.97	75.89	68.04	
Wo	38.24	36.62	4.58	4.26	4.09	
En	54.92	44.99	78.29	72.48	65.87	
Fs	6.83	18.39	17.13	23.26	30.04	
Trace-elements (ppm)						
Ti	2492	6180	1159	1769	2786	
Ti[a]	2698	7194	1259	1978	3897	2.1
Sr	17.6	22.0				
Y	6.4	18.3	1.3	1.9	3.1	4.9
Zr	9.2	31.1	1.7	2.5	6.3	5.4
Cr	6693	340.0	2897	668	205	
Cr[a]	8074	342	3695	479	205	2.2
La	0.53	1.73				
Ce	2.11	6.76				
Nd	2.71	8.32				
Sm	1.07	2.76				
Eu	0.28	0.83				
Dy	1.21	3.14				
Er	0.62	1.51				
Yb	0.51	1.40				

Traces obtained by ion microprobe.
[a] Calculated from electron microprobe analyses.

of Mg–Fe between the ferromagnesian minerals as documented above.

6. Zoning patterns and crystallization processes

Initially, it is important to note that the multiphase saturation of olivine–orthopyroxene–clinopyroxene–plagioclase of the parent magma was probably caused by the assimilation of silicic crustal material such as the host Precambrian gneisses. The presence of >51 wt.% SiO$_2$ in the two samples and their radiogenic Sr isotopes and negative ε_{Nd} support this notion. However, the similar initial isotopic composition of the chilled margin #9010 and the gabbronorite #9011 (Table 1) precludes
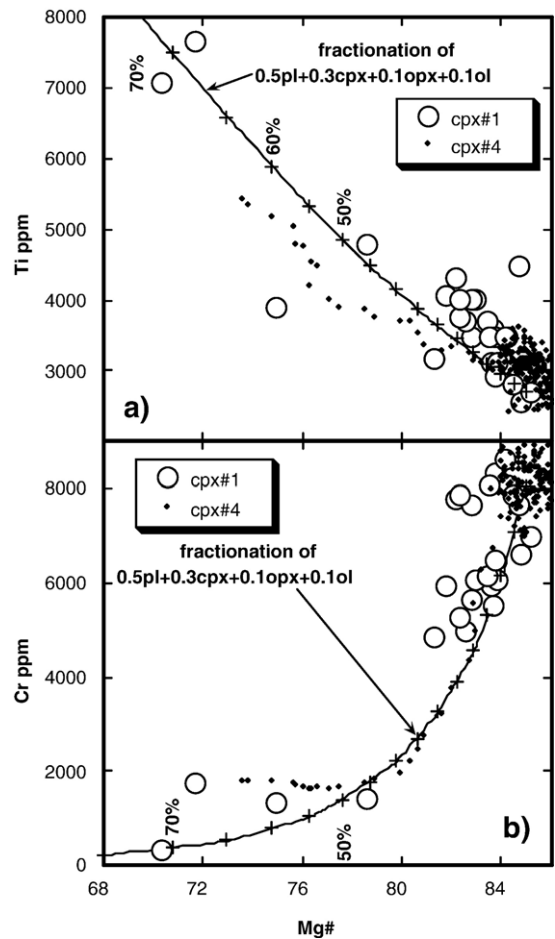

Fig. 4. (a and b) Variation of (a) Ti and (b) Cr with Mg# in clinopyroxene crystals cpx#1 and cpx#4 in gabbronorite #9011. The curves show the result of perfect crystal fractionation of the assemblage of the gabbronorite. Crosses are at 5% fractionation intervals. Distribution coefficients as listed in Table 3. Fractionation of Mg–Fe was calculated following the method described in Bernstein et al. (1996).
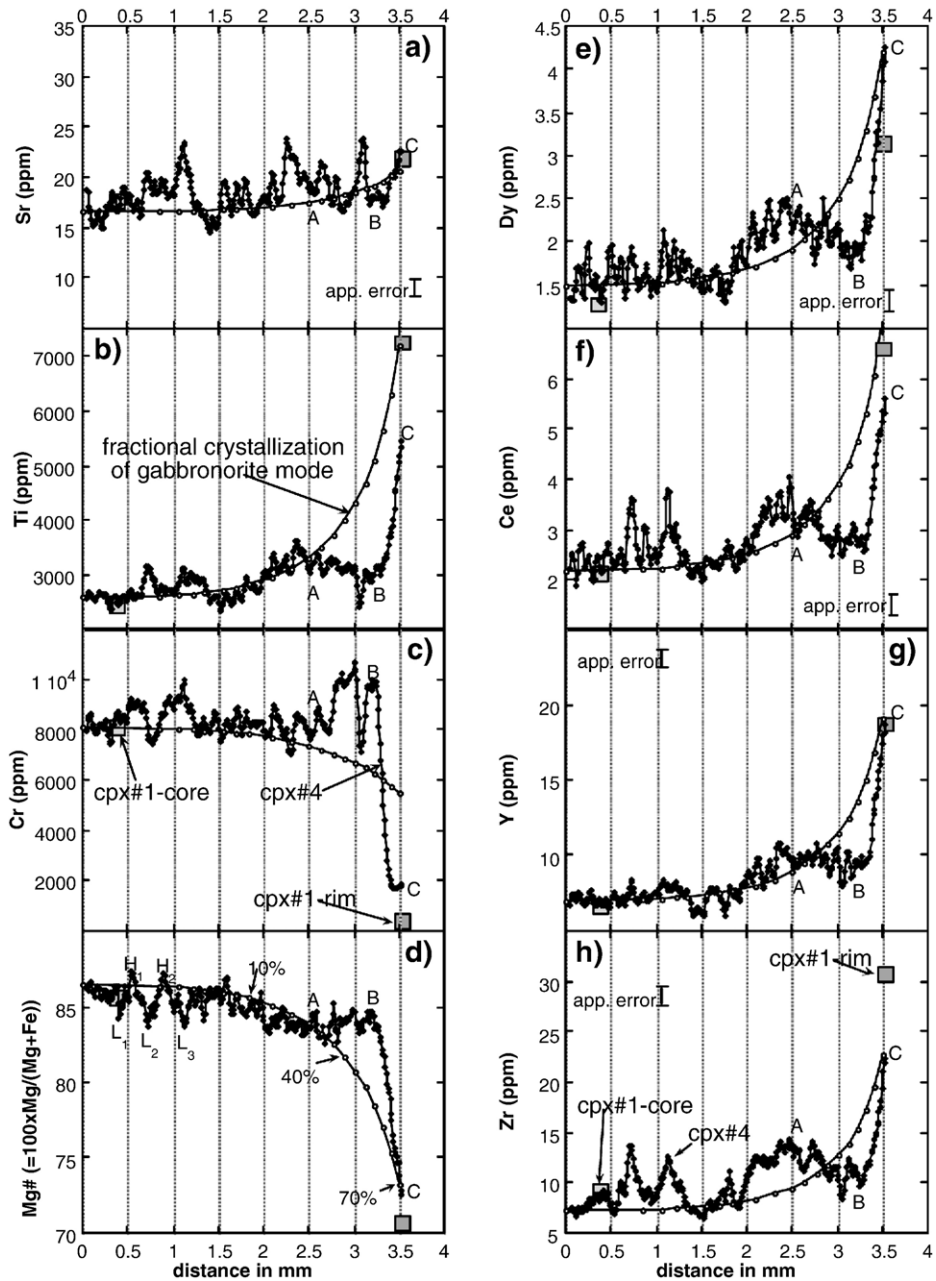
Fig. 5. (a–h) Zonation of Mg# and selected trace elements for clinopyroxene crystal cpx#4, as obtained by LA–ICP–MS line scan (small diamonds). The compositions of cpx#1 core and rim, as obtained by ion microprobe analysis (panel h; Table 2), are also shown (large squares). Approximate error bars are shown except in (b), (c), and (d), where they are only slightly larger than the size of the data points for cpx#1. The trajectories represent modelling of fractionation of the gabbronorite mode as shown in Fig. 4, with 0–4% in 1%, 4–10% in 2%, and 10–70% in 5% increments, respectively (panel d).

significant contamination after emplacement of the pluton. It seems likely that assimilation of gneissic material occurred at deeper levels while the magma was in transit to the upper crustal level at which it was emplaced.

The correlation between Mg# and trace element concentrations in clinopyroxene and orthopyroxene suggests that fractional crystallization was responsible for the observed zonation. This is illustrated in Fig. 4 for clinopyroxene crystals cpx#1 and cpx#4 with modelled

Table 3
Partition coefficients for solid phases/melt

	ol	Ref	opx	Ref	cpx	Ref	plag	Ref	cpx/opx
Ti	0.015	1	0.14	6	0.38	9	0.05	2	2.74
Sr	0.003	2	0.002	7	0.13	9	1.55	10	
Y	0.023	3	0.10	3	0.47	9	0.023	11	4.67
Zr	0.009	4	0.02	8	0.12	9	0.010	12	6.15
Cr	0.73	5	1	8	3.8	9	0.080	8	
La	7×10^{-6}	1	9×10^{-4}	1	0.05	9	0.022	10	
Ce	1×10^{-5}	1	5×10^{-4}	1	0.08	9	0.016	10	
Nd	7×10^{-5}	1	0.009	1	0.19	9	0.014	10	
Sm	7×10^{-4}	1	0.02	1	0.29	9	0.009	10	
Eu	9×10^{-4}	1	0.03	1	0.29	9	0.025	10	
Dy	0.004	1	0.06	1	0.44	9	0.010	10	
Er	0.009	1	0.07	1	0.39	9	0.010	10	
Yb	0.023	1	0.10	1	0.43	9	0.010	10	

References: 1, Kelemen et al. (1993); 2, Irving (1978) and references therein; 3, by analogy with Er and Yb; 4, Larsen (1979); 5, Nikogosian and Sobolev (1997); 6, Kelemen et al. (1993); 7, Kelemen and Dunn (1992); 8, Dunn and Sen (1994); 9, Hart and Dunn (1993); 10, McKay et al. (1994); 11, Bindeman et al. (1998); 12, Fujimaki et al. (1984).

fractionation of the modal composition of the olivine gabbronorite #9011. There is a good fit between the fractionation model and the observed compositions. An almost identical result is obtained by modelling REE, as shown in Fig. 6a. The degree of fractionation from core to rim in cpx#1 is about 70% for both Fe–Mg distribution and for the trace elements, as demonstrated in Figs. 4 and 6. The data points of cpx#4 roughly follow those of cpx#1, but the higher Mg# and lower Ti-content of the cpx#4 rim suggest a somewhat lower degree of fractionation (63%). The Ti-data are offset to slightly lower values for cpx#4 than cpx#1. The Mg#– Cr data of cpx#4 (Fig. 4b) first follow the fractionation path of cpx#1, but during the final stages (Mg# 78– 73.5), the Cr-concentrations flatten out at a constant value of about 1900 ppm.

The same fractionation model is applied to the orthopyroxene crystal opx#2 (Fig. 7), showing that the intermediate portion of the crystal with a Mg# of 75.5 crystallized from a melt which had undergone some 40% fractional crystallization, relative to the crystal core. The rim with a Mg# of 67.6 suggests precipitation from a liquid which had undergone ca. 65% fractionation. The concentrations of Ti and Zr in the rim suggest somewhat higher degree of fractionation (73% and 75%, respectively), but the overall fit to the fractionation model is quite good and in accordance with the estimates of fractionation deduced from the clinopyroxene data presented above.

Whereas the marked zonation patterns in clinopyroxene and orthopyroxene crystal rims can be explained in terms of closed system fractional crystallization, the zonation details of cpx#1 and cpx#4 require closer study (Figs. 3 and 5). The Mg# variations in cpx#1 and cpx#4 (Figs. 3c and 5d) show a series of spikes superimposed on a trend of gentle decrease in Mg# towards the strongly zoned rim. This gentle decrease in Mg# correlates with a broad increase in the incompatible elements Ti, Zr, Y, Ce and Dy and a gentle decrease in Cr and fairly constant Sr values, when disregarding the spikes. As shown in Fig. 5, these patterns are consistent with fractional crystallization of the gabbronorite assemblage given above, and reflecting some 70% crystallization. The distance from core to rim of 3.5 mm in cpx#4 has been converted into volume fraction by
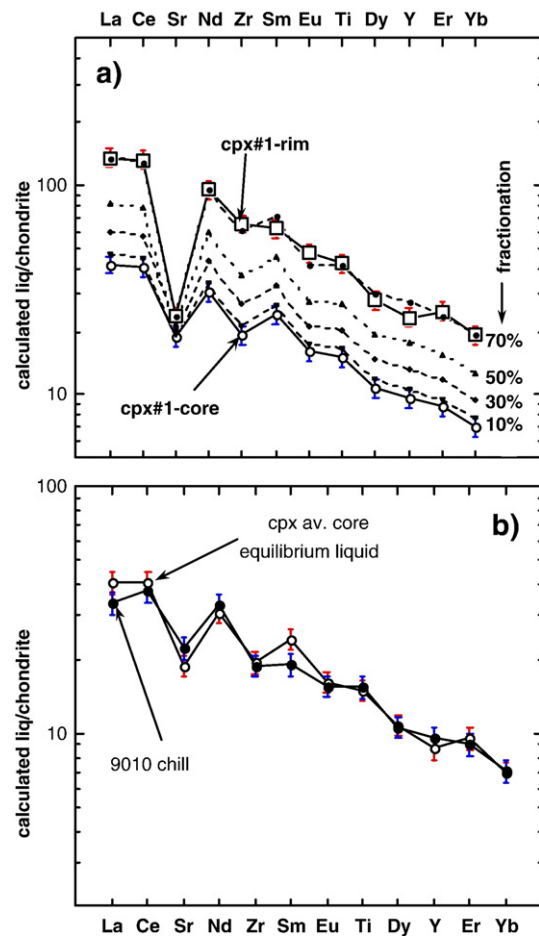

Fig. 6. (a–b) The result of simple fractionation model (a) with the fractionating assemblage of 0.5pl+0.3cpx+0.1opx+0.1ol. The initial liquid is that calculated to be in equilibrium with clinopyroxene cpx#1 core, showing that the rim of cpx#1 crystallized from a melt that had undergone some 70% fractional crystallization. (b) Equilibrium melt composition calculated from cpx#1 core of Tables 1 and 2 using distribution coefficients in Table 3, and compared with the composition of the chilled margin of the gabbronorite plug (#9010). Chondrite normalization factors are from Sun and McDonough (1989).
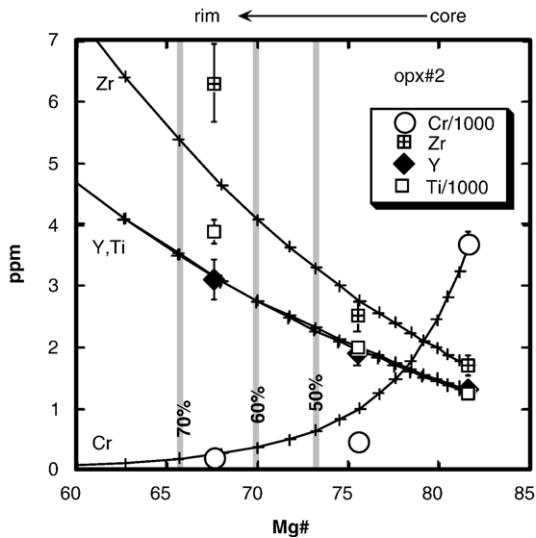
Fig. 7. Compositional zonation in orthopyroxene crystal opx#2 in terms of Mg# and the elements Cr, Ti, Zr, and Y (in ppm). The curves represent fractional crystallization of the assemblage 0.5pl+0.3cpx+ 0.1opx+0.1ol. Tick marks for every 5% fractionation.

considering a sphere with a radius of 3.5 mm. This approximation is based on the observed radial arrangement of the clinopyroxene blades around the fine-grained olivine–orthopyroxene–clinopyroxene–plagioclase centres as described in the Petrography section (Fig. 2).

Spikes in the general trends are found for all the variables portrayed in Fig. 5, with some spikes following a consistent pattern for all elements, while others appear to be restricted to a few elements. For example, the prominent spikes marked L_1–H_1–L_2–H_2–L_3 (low$_1$–high$_1$, etc.) in Fig. 5d are well defined in terms of Mg# and correlate to variable degrees with spikes in the other elements, and can also be identified in the electron-microprobe data (Mg#) of cpx#1 (Fig. 3c). In Fig. 8, the transition from H_1 to L_2 is portrayed by the covariation of certain trace elements with Mg# in cpx#4. Apart from some excursions in the middle portion of the H_1–L_2 transition, there are negative correlations between Mg# and the trace elements Ti, Sr, Y, Zr and Ce and a positive correlation between Mg# and Cr. These variations follow a simple trend of fractional crystallization of the gabbronorite assemblage and mode (0.1ol−0.1opx−0.3cpx−0.5pl) with a maximum of nearly 30% crystallization. Alternatively, about 20% fractionation of a mode of 100% clinopyroxene could yield similarly close modelling of the data for Ti, Y, and Ce, with better fit for Sr, but worse for Cr, which becomes rapidly depleted in the model (Fig.

8f), because of the high K_D (=3.8; Table 3) for clinopyroxene/liquid.

The series of spikes L_1–H_1–L_2–H_2–L_3 (Fig. 5d) can be interpreted in terms of crystallization kinetics, where element diffusion in the melt reservoir was too slow to maintain compositional homogeneity. Considering that the major and trace element data for the H_1–L_2 transition require some 20–30% crystallization, for a crystal volume of only about 0.1% (converting the analysed distance of 0.55–0.75 mm from the crystal core to fraction of a sphere with 3.5 mm radius), this portion of the clinopyroxene crystal must have grown from a minute fraction of the melt. It is interesting to note that after each L-spike, the data return to a baseline level, which follows that of fractional crystallization of the gabbronorite mode for a spherical clinopyroxene crystal (Fig. 5a–h). Therefore the L-spikes could result from periods of rapid crystal growth, where the growth speed exceeded that of liquid state diffusion at a length scale required for maintaining a homogeneous melt reservoir. At the time when the crystal growth reached the L-spike, the rate of crystal growth to liquid state diffusion or convection in the melt reservoir decreased, so that the advancing clinopyroxene crystallization front again was exposed to the bulk melt reservoir, leading to the precipitation of clinopyroxene which was in equilibrium with the bulk melt.

The interpretation of the spikes in Fig. 5a–h to represent periods of rapid crystal growth is supported by the fact that Sr behaves incompatibly like Ce and Zr from H_1–L_2 (Fig. 8b). This requires that the melt from which the clinopyroxene grew did not fractionate plagioclase during this period, supporting the notion of a chemical boundary layer adjacent to the advancing clinopyroxene edge, which thus was temporarily isolated from the bulk melt reservoir. Fractionation of clinopyroxene only is also depicted in Fig. 8 and would reflect the extreme case where the melt only 'sees' the crystallizing clinopyroxene. The excursions to high Cr and low incompatible element concentrations in the interval Mg# 85–86 may suggest a short period where the fractionated melt at the crystallization edge of the clinopyroxene was temporarily replaced by melt from the bulk melt reservoir.

It is apparent from Fig. 5a that there are numerous transient enrichments in Sr, and that they do not always coincide with similar enrichments in other trace elements. However, many of the positive spikes in Sr correlate with positive spikes in Ti and negative spikes in Mg# and Cr (Fig. 5a–d). The oscillatory zoning in clinopyroxene is therefore attributed to a kinetic control,
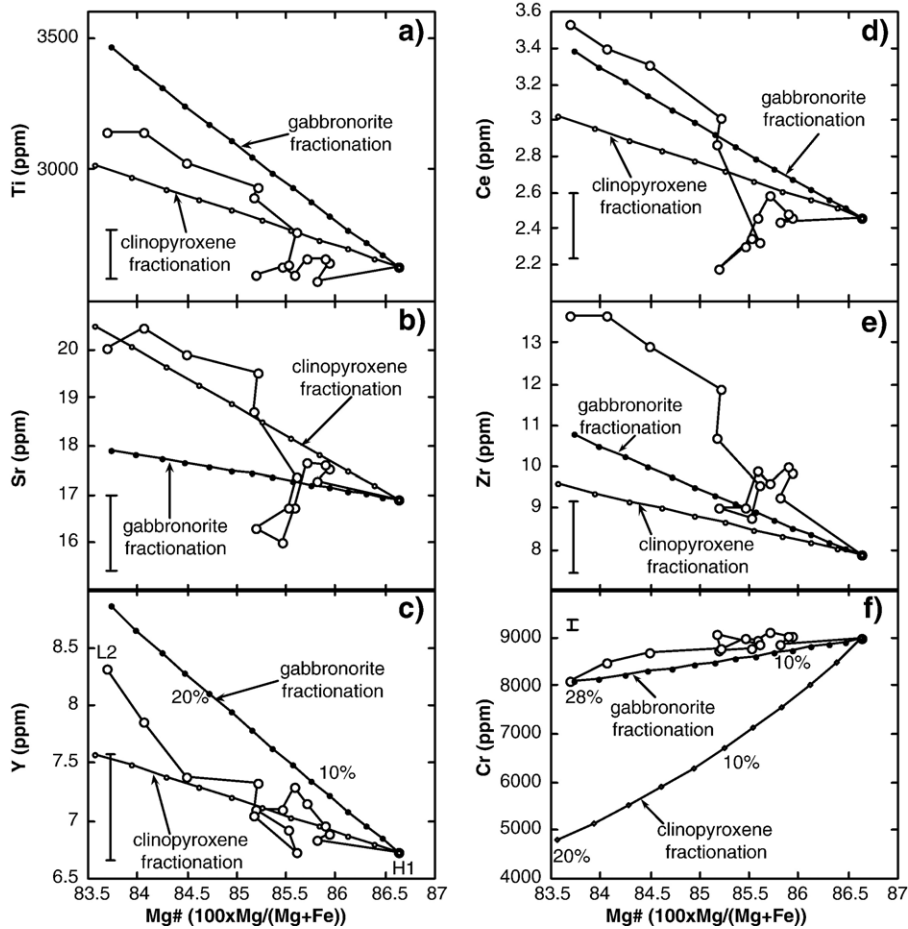
Fig. 8. (a–f) Details of the variation from H_1–L_2 in Fig. 5 for trace elements against Mg# of clinopyroxene crystal cpx#4 (LA–ICP–MS data) shown with large, open circles. Bars give typical analytical errors. Curves represent fractional crystallization of the gabbronorite assemblage (0.5pl + 0.3cpx + 0.1opx + 0.1ol) in 2% increments and of pure clinopyroxene fractionation also in 2% increments. The higher degree of fractionation required for the gabbronorite assemblage compared to the pure clinopyroxene assemblage (28% vs. 20%, respectively) reflects the diluting effect of plagioclase on Fe–Mg fractionation.

as outlined above, and as described for oscillatory zoning in plagioclase by Ginibre et al. (2002).

While this fractionation scheme accounts well for the correlation between Mg# and the elements Y, Ti, Ce, and Sr in the transition H_1–L_2 (Fig. 8), there are quite large deviations for Zr and Cr (Fig. 8e and f). Zirconium is enriched beyond what can be expected by fractional crystallization, even in the unlikely case of a bulk distribution coefficient of zero. Likewise, Cr decreases only slowly. It is interesting to note that an excess enrichment in Zr is also found in the ion-microprobe study of Tribuzio et al. (1999) of clinopyroxene from oceanic gabbros. For a modest decrease in Mg# from core to rim (82 to 79), Tribuzio et al. (1999) found an increase in Ti, Y, and Ce of about 2, 3 and 5.7, respectively, against a nearly 10 times increase in Zr.

This behaviour was ascribed to the coprecipitation of apatite and Fe–Ti oxides with low partition coefficients for Zr, thus lowering the bulk partition coefficient for Zr, while increasing the bulk partition coefficients for Ti and REEs (Tribuzio et al., 1999). An alternative explanation for the apparent decoupling of Zr from other trace elements and Mg/Fe ratio was suggested by Ross and Elthon (1997) who hypothesized that the fast equilibration of Mg–Fe in ferromagnesian silicates outscaled the equilibration of intracrystalline chemical gradients of tetravalent ions such as Zr and Ti. The concentrations of Ti and Zr would therefore more closely reflect the effect of fractional crystallization during crystal growth, whereas Mg–Fe distribution would reflect incomplete homogenization by diffusion (Ross and Elthon, 1997). These models are, however, at

odds with the observation of the frequent oscillation in Mg# throughout the clinopyroxenes (Figs. 3c and 5d). A third, and more likely, possibility is disequilibrium partitioning of Zr during rapid crystal growth (e.g. Albarède and Bottinga, 1972; Hart, 1981; Shimizu, 1981), as in the case of fractional crystallization in the interval H_1–L_2 (Fig. 8). Experimental studies have demonstrated a strong correlation between diffusion coefficient and ionic charge and radius. For instance, the compilation by Hofmann (1980) and the study of Harrison and Watson (1983) show that in a dry silicate melt of basaltic to granitic composition, the tetravalent Zr diffuses at least two orders of magnitude slower than a trivalent REE (Eu). Therefore, in the case of rapid crystal growth, the excluded element Zr (and Ti, Ce and Y, in order of decreasing diffusivity) will tend to pile up against the advancing clinopyroxene crystallization front and will lead to an increase in concentration in the advancing crystal. The limited decrease in Cr from H_1 to L_2 is difficult to account for. Chromium does diffuse much faster than the incompatible elements mentioned above, but considerably slower than Fe–Mg, so it is not possible to explain the high Cr in terms of diffusional fractionation alone.

One additional detail, which is difficult to account for, is the slight enrichment in Cr towards the crystal rim ('A–B' in Fig. 5c). This enrichment in Cr is accompanied by a modest increase in Mg# and marked decrease in the incompatible elements Ti, Dy, Ce, Y, and Zr (Fig. 5). The 'A–B' segment is followed by the marked zonation towards the crystal edge ('B–C') that can be accounted for by fractional crystallization, as discussed above. No impurities were observed in the crystal in the 'A–B' segment, and the possibility of influx of less differentiated melt is excluded because of the identical compositions of the gabbronorite and its chilled margin. However, small-scale (few mm) advection of interstitial liquids could potentially bring melts enriched in Cr to the crystallizing edge of cpx#4. Such enrichment of Cr could arise from plagioclase growth prior to the migration of the melt towards cpx#4. It is interesting to note that the positive spikes in Cr at 2.8–3 mm and at 3.2 mm distance in cpx#4 (x-axis in Fig. 5) coincide with low Sr concentrations, indeed pointing to plagioclase fractionation. Small-scale advection of interstitial liquids, even in a seemingly closed system such as that represented by the gabbronorite, is likely to occur because of the volume reduction from liquid to solid state. This process is referred to as 'solidification contraction' (e.g. Petersen, 1987) and is most efficient towards the final stage of crystallization, when the area of crystal surfaces is large compared to the volume of liquid.

There is a more marked decrease in Cr in the segment 'B–C' (Fig. 5c) than can be accommodated by fractionation of the gabbronorite assemblage, but occurrence of interstitial, euhedral spinel grains (Fig. 2b) suggests that spinel joined the fractionation assemblage at an advanced degree of crystallization, resulting in increased bulk K_D for Cr.

Fractional crystallization of plagioclase, clinopyroxene, orthopyroxene and olivine in the proportions present in the gabbronorite can therefore account for some 70% crystallization as recorded by the zonation of the clinopyroxene and orthopyroxene grains. The remaining 30% of the crystallization path is not recorded in the data, but petrographic observations suggest that, at the stage of ca. 70% solidification, the residual melt was residing in pockets where the final crystallization took place with precipitation of biotite, amphibole and Fe–Ti oxides in addition to pyroxene and plagioclase (Fig. 2d).

This simple fractionation model requires that the fractionation mode of 0.5pl + 0.3cpx + 0.1opx + 0.1ol remained essentially unchanged during some 70% crystallization, which perhaps is somewhat surprising. On the other hand, the closely similar degree of Mg# zonation in olivine, orthopyroxene and clinopyroxene and of An# in plagioclase (Fig. 3), and the petrographic evidence of large, zoned crystals of all four phases, support the notion of coprecipitation of the three ferromagnesian silicates and plagioclase throughout the solidification of the rock.

7. Compositions of calculated melt and chilled margin

It is assumed that the composition of the chilled margin is representative of melt parental to the gabbronorite. The trace element composition of the cpx#1 core has been used to calculate the equilibrium melt composition using the distribution coefficients listed in Table 3. The result is listed in Table 1 and illustrated in Fig. 6b. In general there is very good agreement between the composition of the chilled margin sample and the composition of the calculated equilibrium melt, with deviations from the chilled margin composition of less than 10% for most elements. Exceptions are Sr (underestimated by 16%) and La and Sm, which are overestimated by 20% and 27%, respectively, in the calculated melt. When considering that the errors on both analytical methods (whole-rock ICP–MS and ion-microprobe on clinopyroxene) are about 10% for trace elements, the difference in trace element concentrations between the chilled margin

sample and the calculated equilibrium melt is within this error for Sr and just outside the error for the elements La and Sm, as illustrated by the error bars in Fig. 6b.

While the trace element composition of the calculated equilibrium melt thus is in accordance with the chilled margin composition, this does not apply to the Mg# of the calculated melt. The highest measured Mg# of a clinopyroxene core is 85.8, and given a K_D of 0.26 (Grove and Bryan, 1983) the parental melt should have Mg# around 61. This value is much lower than the Mg# of 75.7 of the chilled margin #9010 (calculated using $FeO = 0.9 * FeO^{total}$). Some of this difference could stem from uncertainty of the Fe–Mg partitioning between clinopyroxene and melt, but even for a K_D of 0.28 (which is on the high side of reported K_D values) the equilibrium melt would still only have a Mg# of about 63. One likely reason for this mismatch could be accumulation of olivine and orthopyroxene crystals in the chilled margin (and/or in the gabbronorite sample). If the clusters of small olivine and orthopyroxene crystals in chilled margin sample #9010 are interpreted as accumulated material, then the Mg# of #9010 decreases from 75.7 to about 68 after extraction of 20% of 1:1 olivine–orthopyroxene accumulation with the composition given above. This would require accumulated olivine and orthopyroxene crystals to be distributed evenly throughout the magma during and after emplacement, because of the close chemical resemblance of bulk samples #9010 and #9011. Observation of evenly distributed phenocrysts in lava flows is very common, rendering crystal accumulation a plausible explanation for some of the observed discrepancy in Mg# between bulk rock and crystal cores. Indeed, the higher Cr and Ni (3330 and 370 ppm, respectively) in the gabbronorite sample #9011, compared to the chilled margin sample #9010 can be explained by slightly higher contents of pyroxene-, olivine- or Cr-rich spinel microphenocrysts in the gabbronorite magma prior to the onset of in situ crystallization.

Another possibility that potentially would lower the Mg# of crystal cores from the gabbronorite is post-crystallization equilibration of intracrystal Mg–Fe gradients, as proposed by Ross and Elthon (1997). Subsequent to the crystallization of mineral grains, the temperatures within the gabbronorite plug may have been high enough for Fe–Mg diffusion through the crystal. The limit for this process to be active is the cooling time from magmatic temperatures to the ambient host-rock temperature where solid-state Fe–Mg diffusion is effectively stopped. The chemical zoning in olivine (Fig. 3a) suggests that post-crystallization Fe–Mg diffusion was insignificant, since interdiffusion coeffi-

cient for Fe–Mg exchange in olivine is several orders of magnitude faster than in pyroxenes (Freer, 1981). In fact, the preservation of zoning in olivine suggests fast cooling rates for the gabbronorite plug.

One final explanation is solid–liquid disequilibrium during rapid crystal growth. In a silicate melt, distribution coefficients for network forming species, such as MgO and FeO, approach unity at increasing and high crystal growth rates. In the present case, the clinopyroxene/liquid Fe/Mg is 0.52, and significantly higher than the experimental value of 0.26 (Grove and Bryan, 1983), but similar to the values reported from quenched olivine from impact melts for e.g. olivine (K_D olivine/melt of 0.54–0.73; Hörz and See, 2000), that result from disequilibrium crystallization. However, one complication to the application of disequilibrium crystallization in the present case is that Fe/Mg exchange between the ferromagnesian minerals olivine, clinopyroxene and orthopyroxene in sample #9011 is close to values reported from slowly cooled mafic intrusions. For the crystal cores of olivine #1 and clinopyroxene #1 (Fig. 3) in gabbronorite #9011, Fe/Mg for olivine/clinopyroxene and olivine/orthopyroxene is 1.42 and 1.32, respectively. The corresponding values from Fongen–Hyllingen intrusion (Norway) are 1.53 and 1.34 (Wilson et al., 1981); from the Skaergaard Intrusion (Greenland): 1.61–1.8 and 1.36–1.48 (Peter Thy, personal communication, 2005); and from the Kap Edvard Holm Complex (Greenland): 1.48 for olivine/clinopyroxene (Bernstein et al., 1992). It is thus concluded that the ferromagnesian minerals in the gabbronorite crystallized in mutual equilibrium, and therefore also in equilibrium with the melt.

In the light of the discussion above, crystal accumulation before the onset of in situ crystallization is the preferred explanation for the discrepancy in Mg# of the chilled margin compared with the Mg# in ferromagnesian minerals.

8. Conclusions

Crystallization of the gabbronorite as recorded by major and trace element distribution in clinopyroxene and orthopyroxene can be described in terms of closed system fractional crystallization. The crystallizing assemblage consisted of plagioclase, clinopyroxene, olivine and orthopyroxene in the proportions defined by the mode of the gabbronorite, perhaps with the addition of Fe-spinel during the final stage of crystallization. This assemblage can account for at least 70% crystallization.

Oscillatory zoning in clinopyroxene appears to be a result of crystallization kinetics, where the growth speed

of the clinopyroxene occasionally exceeded that of liquid state diffusion and resulted in a chemical boundary layer separating the advancing crystal face from the bulk melt reservoir.

The composition of the chilled margin of the gabbronorite can be reproduced within the errors of trace element analysis by inverting measured compositions of the clinopyroxene cores from the gabbronorite. This study therefore provides a quantitative confirmation of the calculated equilibrium melt method in estimating the composition of melt parental to intrusive rocks. It is, however, uncertain as to what degree this approach can be applied to slowly cooled plutons, where the composition of cumulus phases can be severely affected by equilibration with evolved, interstitial melts (see e.g. Cawthorn, 1996b). Such post cumulus equilibration may have profound consequences on the composition of the calculated equilibrium melt, if based upon trace element analyses of cumulus crystals. The successful application of the method of calculated equilibrium melt composition based on crystal core analyses therefore requires that the crystals show some degree of Fe–Mg zoning, which constrains potential post-cumulus equilibration with interstitial melts.

Acknowledgments

References

Albarède, F., Bottinga, Y., 1972. Kinetic disequilibrium in trace element partitioning between phenocrysts and host lava. Geochim. Cosmochim. Acta 36, 141–156.

Barnes, S.J., 1986. The effect of trapped liquid crystallization on cumulus mineral compositions in layered intrusions. Contrib. Mineral. Petrol. 93, 524–531.

Barnes, S.J., 1989. Are Bushveld U-type parent magmas boninites or contaminated komatiites? Contrib. Mineral. Petrol. 101, 447–457.

Bédard, J.H., 1994. A procedure for calculating the equilibrium distribution of trace elements among the minerals of cumulate rocks, and the concentration of trace elements in the coexisting liquids. Chem. Geol. 118, 143–153.

Benoit, M., Polvé, M., Ceuleneer, G., 1996. Trace element and isotopic characterization of mafic cumulates in a fossil mantle diapir (Oman ophiolite). Chem. Geol. 134, 199–214.

Bernstein, S., Rosing, M.T., Brooks, C.K., Bird, D.K., 1992. An ocean-ridge type magma chamber at a passive volcanic, continental margin: the Kap Edvard Holm layered gabbro complex, East Greenland. Geol. Mag. 129, 437–456.

Bernstein, S., Kelemen, P.B., Brooks, C.K., 1996. Evolution of the Kap Edvard Holm Complex: a mafic intrusion at a rifted continental margin. J. Petrol. 37, 497–519.

Bernstein, S., Kelemen, P.B., Tegner, C., Kurz, M.D., Blusztajn, J., Brooks, C.K., 1998. Post break-up basaltic magmatism along the East Greenland Tertiary rifted margin. Earth Planet. Sci. Lett. 160, 845–862.

Bindeman, I.N., Davis, A.M., Drake, M.J., 1998. Ion microprobe study of plagioclase–basalt partition experiments at natural concentration levels of trace elements. Geochim. Cosmochim. Acta 62, 1175–1193.

Brey, G.P., Köhler, T., 1990. Geothermobarometry in four-phase lherzolites: II. New thermobarometers, and the practical assessment of existing thermobarometers. J. Petrol. 31, 1353–1378.

Brooks, C.K., Nielsen, T.F.D., 1978. Early stages in the differentiation of the Skaergaard magma as revealed by a closely related suite of dyke rocks. Lithos 11, 1–14.

Cawthorn, R.G. (Ed.), 1996a. Layered Intrusions. Developments in Petrology, vol. 15. Elsevier, Amsterdam, p. 542.

Cawthorn, R.G., 1996b. Models for incompatible trace-element abundances in cumulus minerals and their application to plagioclase and pyroxenes in the Bushveld Complex. Contrib. Mineral. Petrol. 123, 109–115.

Dunn, T., Sen, C., 1994. Mineral/matrix partition coefficients for orthopyroxene, plagioclase, and olivine in basaltic to andesitic systems: a combined analytical and experimental study. Geochim. Cosmochim. Acta 58, 717–733.

Eggins, S.M., Rudnick, R.L., McDonough, W.F., 1998. The composition of peridotites and their minerals, a laser ICP–MS study. Earth Planet. Sci. Lett. 154, 53–71.

Freer, R., 1981. Diffusion in silicate minerals and glasses: a data digest and guide to the literature. Contrib. Mineral. Petrol. 76, 440–454.

Fujimaki, H., Tatsumoto, M., Aoki, K., 1984. Partition coefficients of Hf, Zr, and REE between phenocrysts and groundmasses. J. Geophys. Res. 89, B662–B672.

Ginibre, C., Wörner, G., Kronz, A., 2002. Minor- and trace-element zoning in plagioclase: implications for magma chamber processes at Parinacota Volcano, northern Chile. Contrib. Mineral. Petrol. 143, 300–315.

Grove, T.L., Bryan, W.B., 1983. Fractionation of pyroxene-phyric MORB at low pressure: an experimental study. Contrib. Mineral. Petrol. 84, 293–309.

Harnois, L., Trottier, J., Morency, M., 1990. Rare earth element geochemistry of Thetford Mines ophiolite complex, Northern Appalachians, Canada. Contrib. Mineral. Petrol. 105, 433–445.

Harrison, T.M., Watson, E.B., 1983. Kinetics of zircon dissolution and zirconium diffusion in granitic melts of variable water content. Contrib. Mineral. Petrol. 84, 66–72.

Hart, S.R., 1981. Diffusion compensation in natural silicates. Geochim. Cosmochim. Acta 45, 279–291.

Hart, S.R., Dunn, T., 1993. Experimental cpx/melt partitioning of 24 trace elements. Contrib. Mineral. Petrol. 113, 1–8.

Hofmann, A.W., 1980. Diffusion in natural silicate melts: a critical review. In: Hargraves, R.B. (Ed.), Physics of Magmatic Processes. Princeton University Press, Princeton, pp. 385–418.

Hoover, J.D., 1978. Melting relations of a new chilled margin sample from the Skaergaard intrusion. Carnegie Inst. Wash. Yearb. 77, 739–743.

Hörz, F., See, T.H., 2000. Quenched olivines and pyroxenes in impact melts from Meteor Crater, AZ. In: Proc. 31st. Lunar Sci. Conf. 1737.pdf.

Irving, A.J., 1978. A review of experimental studies of crystal/liquid trace element partitioning. Geochim. Cosmochim. Acta 42, 743–770.

Kays, M.A., Goles, G.G., Grover, T.W., 1988. Precambrian sequence bordering the Skaergaard Intrusion. J. Petrol. 30, 321–361.

Kelemen, P.B., Dunn, T., 1992. Depletion of Nb relative to other highly incompatible elements by melt/rock reaction in the upper mantle. Eos 656–657.

Kelemen, P.B., Shimizu, N., Dunn, T., 1993. Relative depletion of niobium in some arc magmas and the continental crust: partitioning of K, Nb, La and Ce during melt/rock reaction in the upper mantle. Earth Planet. Sci. Lett. 120, 111–134.

Kelemen, P.B., Koga, K., Shimizu, N., 1997. Geochemistry of gabbro sills in the crust–mantle transition zone of the Oman ophiolite: implications for the origin of the oceanic lower crust. Earth Planet. Sci. Lett. 146, 475–488.

Kystol, J., Larsen, L.M., 1999. Analytical procedures in the Rock Geochemical Laboratory of the Geological Survey of Denmark and Greenland. Geol. Greenl. Surv. Bull. 184, 59–62.

Larsen, L.M., 1979. Distribution of REE and other trace elements between phenocrysts and peralkaline undersaturated magmas, exemplified by rocks from the Gardar igneous province, South Greenland. Lithos 12, 303–315.

McBirney, A.R., 1998. The Skaergaard Layered Series: Part V. Included trace elements. J. Petrol. 39, 255–276.

McKay, G., Le, L., Wagstaff, J., Crozaz, G., 1994. Experimental partitioning of rare earth elements and strontium: constraints on petrogenesis and redox conditions during crystallization of Antarctic angrite Lewis Cliff 86010. Geochim. Cosmochim. Acta 58, 2911–2919.

Nikogosian, I.K., Sobolev, A.V., 1997. Ion-microprobe analysis of melt inclusions in olivine: experience in estimating the olivine–melt partition coefficients of trace elements. Geochem. Int. 35, 119–126.

Normann, M.D., 1998. Melting and metasomatism in the continental lithosphere: laser ablation ICPMS analysis of minerals in spinel lherzolites from eastern Australia. Contrib. Mineral. Petrol. 130, 240–255.

Parsons, I. (Ed.), 1987. Origins of Igneous Layering. Reidel Publishing Company, Dordrecht, p. 666.

Petersen, J.S., 1987. Solidification contraction: another approach to cumulus processes and the origin of igneous layering. In: Parsons, I. (Ed.), Origin of Igneous Layering. Reidel Publishing Company, Dordrecht, pp. 505–526.

Ross, K., Elthon, D., 1997. Cumulus and postcumulus crystallization in the oceanic crust: major- and trace-element geochemistry of Leg 153 gabbroic rocks. Proc. Ocean Drill. Prog., Sci. Results 153, 333–350.

Shimizu, N., 1981. Trace element incorporation into growing augite phenocryst. Nature 289, 575–577.

Shimizu, N., Hart, S.R., 1982. Applications of the ion micro-probe to geochemistry and cosmochemistry. Annu. Rev. Earth Planet. Sci. 10, 483–526.

Sun, S.-s., McDonough, W.F., 1989. Chemical and isotopic systematics of oceanic basalts: implications for mantle composition and processes. Spec. Publ.-Geol. Soc. Lond., vol. 42, pp. 313–345.

Tegner, C., Wilson, J.R., Brooks, C.K., 1993. Intraplutonic quench zones in the Kap Edvard Holm layered gabbro complex, East Greenland. J. Petrol. 34, 681–710.

Tribuzio, R., Tiepolo, M., Vannucci, R., Bottazzi, P., 1999. Trace element distribution within olivine-bearing gabbros from the Northern Apennine ophiolites (Italy): evidence for post-cumulus crystallization in MOR-type gabbroic rocks. Contrib. Mineral. Petrol. 134, 123–133.

Vannucci, R., Rampone, E., Piccardo, G.B., Ottolini, L., Bottazzi, P., 1993. Ophiolitic magmatism in the Ligurian Tethys: an ion microprobe study of basaltic clinopyroxenes. Contrib. Mineral. Petrol. 115, 123–137.

Wager, L.R., 1947. Geological investigations in East Greenland: Part IV. The stratigraphy and tectonics of Knud Rasmussens Land and the Kangerdlugssuaq region. Medd. Grønl. 134, 1–64.

Wager, L.R., 1960. The major element variation of the layered series of the Skaergaard Intrusion and a re-estimation of the average composition of the hidden layered series and of the successive residual magmas. J. Petrol. 1, 364–398.

Wager, L.R., Brown, G.M. (Eds.), 1968. Layered Igneous Rocks. Oliver & Boyd, Edinburgh, p. 588.

Wager, L.R., Deer, W.A., 1939. Geological investigations in East Greenland: Part III. The petrology of the Skaergaard intrusion, Kangerdlugssuaq, East Greenland. Medd. Grønl. 105, 1–335.

Wilson, J.R., Esbensen, K.H., Thy, P., 1981. Igneous petrology of the sysorogenic Fongen–Hyllingen layered basic complex, South-central Scandinavian. Caledonides 22, 584–627.